Drift-Alfvén fluctuations associated with a narrow pressure striation

J. R. Peñano,[a] G. J. Morales, and J. E. Maggs
Department of Physics and Astronomy, University of California, Los Angeles, California 90095

(Received 10 June 1999; accepted 20 September 1999)

This analytical and numerical study illustrates the linear stability properties of low frequency electromagnetic eigenmodes driven by field-aligned pressure striations whose scale transverse to the confining magnetic field is on the order of the electron skin-depth. A full electromagnetic formulation is given in terms of the coupling of the fluctuating axial fields $(\tilde{E}_z, \tilde{B}_z)$ and incorporates shear and compressional Alfvén waves, drift waves, and ion acoustic waves. The kinetic response of the electrons includes pitch-angle scattering (Lorentz model) and the ions are treated as a magnetized, cold fluid. Detailed quantitative comparisons of the theoretical predictions are made with laboratory observations of fluctuations generated in controlled pressure depletions [J. E. Maggs and G. J. Morales, Phys. Plasmas **4**, 290 (1997)] and in narrow temperature plumes [A. T. Burke, J. E. Maggs, and G. J. Morales, Phys. Rev. Lett. **81**, 3659 (1998)]. © *2000 American Institute of Physics.* [S1070-664X(00)01101-0]

I. INTRODUCTION

It is frequently observed that magnetized plasmas that are far from thermal equilibrium (e.g., naturally occurring plasmas,[1–3] or plasmas in auxiliary heated confinement devices[4,5]) tend to develop microscopic filamentary structures (striations) whose transverse scale is small compared to their extent along the confining magnetic field. By microscopic it is meant that the transverse scale is comparable to the electron skin-depth c/ω_{pe} (where c is the speed of light and ω_{pe} is the electron plasma frequency) or the ion gyroradius, depending on which is larger. The structures can consist of local depletions or enhancements in density and/or temperature and thus be visualized as pressure striations embedded in an otherwise infinite plasma.

It is of interest to examine the stability properties of narrow pressure striations because the resulting fluctuations may have important consequences for the behavior of the surrounding macroscopic plasma. For instance, the parallel electric field associated with the fluctuations can give rise to the acceleration of electrons along the magnetic field and the narrow transverse gradients of the electric fields can cause the formation[6] of energetic ion tails in the perpendicular direction. Both of these processes are presently the subject of intensive studies in connection to rocket and spacecraft observations in the auroral ionosphere and may also have relevance to the behavior of toroidal confinement devices used in fusion research.

This analytical and numerical study has several goals. It first aims to provide an analytical formulation of the linear stability of drift-Alfvén modes in narrow pressure striations having density and/or temperature variations across the confining magnetic field. Emphasis is placed on the kinetic response of the electrons and thus the formulation incorporates pitch-angle scattering collisions[7] (Lorentz model). The ion response is taken to be that of a cold, magnetized fluid. The description used is fully electromagnetic and is based on the coupling of the parallel electric and magnetic fields (E_z, B_z) which are the quantities often neglected in descriptions of related phenomena that are based on the potential formulation (ϕ, A_z). The approach used here automatically describes several modes (shear and compressional Alfvén waves, electrostatic drift waves, ion acoustic waves) which may be coupled to each other through the gradients in density and temperature. The formulation can also be used to describe the scattering and direct conversion[8–10] induced by pressure striations, although no specific examples of these events are presented here.

Another goal of this study is to compare the predictions of the full electromagnetic formulation against detailed observations of density and magnetic fluctuations that spontaneously develop in controlled striations generated in the Large Plasma Device (LAPD)[11] at the University of California, Los Angeles. In these experiments, two different types of narrow pressure striations can be generated (using different techniques). One type consists of a simultaneous depletion in density and in electron temperature[12] and the other type consists of a pure temperature increase[13] (i.e., a heat plume). In addition to providing valuable insight into the interpretation of the LAPD studies, the numerical results presented use the characteristic parameters of these experiments (see Table I) to concretely elucidate the fundamental properties of the various modes that can be spontaneously excited in narrow pressure striations.

It should be noted that in a previous study we considered a limited formulation of purely electrostatic drift modes in pressure striations. Since these modes are automatically included in the general electromagnetic description presented here, it is also of interest to delineate what differences and similarities exist between the two approaches for the conditions prevailing in the LAPD experiments.

[a]Present address: Plasma Physics Division, Code 6794, Naval Research Laboratory, Washington, D.C. 20375. Electronic mail: penano@ppdu.nrl.navy.mil

TABLE I. Parameters used to model plasma conditions in the LAPD for the striation (Ref. 12) and beam (Ref. 13) experiments. Values represent ambient plasma conditions outside the striation/temperature plume for a Helium plasma.

	Striation exp.	Beam exp.
n_0 (plasma density in 10^{12} cm^{-3})	2.6	1.5
T_e (electron temperature in eV)	11.6	0.45
T_i (ion temperature in eV)	0	0
B_0 (magnetic field in kG)	1.0	1.0
$\overline{v_e}$ (electron thermal velocity in cm/s)	1.4×10^8	2.8×10^7
v_A (Alfvén velocity in cm/s)	6.8×10^7	8.9×10^7
c/ω_{pe} (electron skin depth in cm)	0.33	0.43
$\Omega_i/2\pi$ (ion gyrofrequency in kHz)	380	380
ν_{ei} (collision rate in 10^6 s^{-1})	1.6	77

The manuscript is organized as follows. The general electromagnetic formulation is presented in Sec. II. A local analysis of the coupled field equations is used to extract the generic features of the various modes driven by density gradients (Sec. III A) and temperature gradients (Sec. III B). Section IV describes the properties and parameter dependences of the eigenmodes associated with pure density striations (Sec. IV A) and with pure temperature striations (Sec. IV B). In Sec. V a detailed comparison is made between theoretical predictions and experimental observations. Conclusions are presented in Sec. VI. Appendix A summarizes the collisional electron response and Appendix B establishes the connection between the full electromagnetic description and the usual potential formulation (ϕ, A_z).

II. FORMULATION

In this section a system of equations is obtained to describe the linear stability of electromagnetic fields associated with drift-Alfvén waves localized in an axially symmetric pressure striation. A cylindrical coordinate system (r,θ,z) is used in which the striation is centered at $r=0$ with its symmetry axis parallel to $\hat{z}$. The confining magnetic field, $\mathbf{B}_0 = B_0\hat{z}$ is uniform and the surrounding plasma is assumed to be infinite in extent.

The striation is characterized by a radially varying plasma density, $n_0(r)$ and electron temperature, $T_e(r)$. In the numerical studies of relevance to the LAPD experiments the pressure striation consists of a region of depleted density in which the electron temperature is colder than the surrounding plasma (i.e., $\partial_r n_0>0$, $\partial_r T_e>0$). In contrast, the temperature striation consists of a localized temperature enhancement within which the plasma density is uniform (i.e., $\partial_r n_0=0$, $\partial_r T_e<0$).

The small amplitude perturbations have the functional form $\tilde{A}=A_1(r)\exp[i(m\theta+k_z z-\omega t)]+$c.c. with $\omega\ll\Omega_i$. Here, $\Omega_i=eB_0/(Mc)$ is the ion cyclotron frequency, M is the ion mass, and e is the quantum of charge.

The perturbed electric and magnetic fields $\tilde{\mathbf{E}}$ and $\tilde{\mathbf{B}}$ satisfy

$$\nabla\times\tilde{\mathbf{E}}=ik_0\tilde{\mathbf{B}}, \tag{1}$$

$$\nabla\times\tilde{\mathbf{B}}=-ik_0\tilde{\mathbf{E}}+\frac{4\pi}{c}\tilde{\mathbf{j}}, \tag{2}$$

where $k_0=\omega/c$ is the vacuum wave number and $\tilde{\mathbf{j}}$ represents the perturbed current density. The term $-ik_0\tilde{\mathbf{E}}$ in Eq. (2) is usually not retained in the treatment of Alfvén waves but is kept here for the proper treatment of ion acoustic fluctuations. Substituting Eq. (2) into the curl of Eq. (1) results in a wave equation for the electric field

$$\nabla\times(\nabla\times\tilde{\mathbf{E}})-k_0^2\tilde{\mathbf{E}}=ik_0\frac{4\pi}{c}\tilde{\mathbf{j}}. \tag{3}$$

In calculating the perturbed current density to be used in Eq. (3), it is assumed that the perpendicular plasma response is that of a cold fluid. In the relevant low frequency limit, the ion and electron $\mathbf{E}\times\mathbf{B}$ drifts cancel so that there is no Hall current. Also, the electron polarization drift is neglected so that the perpendicular current density is due to the ion polarization drift

$$\mathbf{j}_{1\perp}=-\frac{i\omega}{4\pi}\left(\frac{\omega_{pi}}{\Omega_i}\right)^2\mathbf{E}_{1\perp}, \tag{4}$$

where $\omega_{pi}=\sqrt{4\pi n_0 e^2/M}$ is the ion plasma frequency. While in fluid descriptions the electron diamagnetic current is included explicitly, in this study the equivalent contribution is obtained from a kinetic calculation which results in the generalized diamagnetic frequency given by Eq. (9).

The electron response is derived from a linearized drift-kinetic equation[14] with a Lorentz collision operator[7]

$$i(k_z v_z-\omega)f_{1e}+\nabla_\perp\cdot(\mathbf{v}_{1\perp}f_{0e})-\frac{e}{m}E_{1z}\frac{\partial}{\partial v_z}f_{0e} = -\nu(v,r)\frac{\partial}{\partial\mu}\left[(1-\mu^2)\frac{\partial f_{1e}}{\partial\mu}\right], \tag{5}$$

where $\nu(v,r)=-\nu_{ei}(\sqrt{2}\overline{v_e}/v)^3$ and $\nu_{ei}=2\pi n_0 e^4\Lambda/[m^2\times(\sqrt{2}\overline{v_e})^3]$ is the electron–ion collision frequency. The quantity μ represents the cosine of the velocity pitch angle, i.e., $v_z=v\mu$ where v is the magnitude of the velocity. The Lorentz operator describes the elastic scattering of electrons from ions and is necessary to accurately model the conditions of the LAPD experiments.

The quantity $\mathbf{v}_{1\perp}$ is the guiding center velocity of an electron in the presence of oscillating electromagnetic fields and is given by

$$\mathbf{v}_{1\perp}=\frac{\mathbf{E}_1\times\hat{z}}{B_0}c+\frac{\mathbf{B}_{1\perp}}{B_0}v_z. \tag{6}$$

The first term represents the $\mathbf{E}\times\mathbf{B}$ drift associated with the wave electric field. The second term is a purely electromagnetic contribution which represents the velocity perpendicular to B_0 acquired by a particle that streams along a perturbed magnetic field line.

The zero-order distribution of electron guiding centers is taken to be a Maxwellian with radially varying density and temperature, i.e.,

$$f_{0e}=\frac{n_0(r)}{(2\pi\overline{v}_e^2)^{3/2}}\exp\left(-\frac{v^2}{2\overline{v}_e^2}\right), \tag{7}$$

where $\overline{v}_e(r)=\sqrt{T_e(r)/m}$ is the electron thermal velocity and m is the electron mass. The parallel ion response is assumed to be that of a collisionless cold fluid (retained so that ion acoustic waves are contained in the general formulation).

Using Eq. (5), the following expression for the oscillating parallel current density is obtained (see Appendix A):

$$j_{1ze}+j_{1zi}=j_{1z}=\frac{i\omega}{4\pi}E_{1z}\left[\left(\frac{\omega_{pi}}{k_z c_s}\right)^2\frac{\omega_*}{\omega}+\left(\frac{\omega_{pi}}{\omega}\right)^2+\left(\frac{\omega_{pe}}{\omega}\right)^2\zeta_e^2 Z_N(\zeta_e,\overline{\nu})\right], \tag{8}$$

where

$$\omega_*=\frac{k_\theta c_s^2}{\Omega_i}\left[\frac{1}{2}Z_N(\zeta_e,\overline{\nu})\frac{\partial}{\partial r}\ln n_0(r)+\frac{1}{2}Z_T(\zeta_e,\overline{\nu})\frac{\partial}{\partial r}\ln T_e(r)\right], \tag{9}$$

is a generalized diamagnetic drift frequency, and $c_s=\sqrt{T_e(r)/M}$ is the ion acoustic speed.

The functions Z_N and Z_T which characterize the collisional plasma response to density and temperature gradients can be written as

$$\begin{pmatrix}Z_N(\zeta_e,\overline{\nu})\\ Z_T(\zeta_e,\overline{\nu})\end{pmatrix}\rightarrow\frac{-8}{\sqrt{\pi}}\int_0^\infty\frac{t^2\exp(-t^2)dt}{1-3\zeta_e^2/t^2-i6\overline{\nu}\zeta_e/t^5+6\zeta_e(a_2/a_1)/(5t)}\times\begin{pmatrix}1\\ t^2-(3/2)\end{pmatrix}, \tag{10}$$

where $\overline{\nu}=\nu_{ei}/(\sqrt{2}k_z\overline{v}_e)$ and $\zeta_e=\omega/(\sqrt{2}k_z\overline{v}_e)$ are the scaled collision frequency and phase velocity, respectively. The ratio a_2/a_1 corresponds to a continued fraction defined by Eq. (A13). The continued fraction approach is useful in the limit of strong collisionality because, numerically, the iteration converges rapidly. However, convergence is very slow as ν_{ei} is made small.

Alternatively, the collisionless counterpart of Eq. (8) can be derived by simply neglecting the collision operator in Eq. (5), solving for f_{1e} and applying $-e\int d^3v v_z$. The result is identical in form to Eq. (8), but with Z_N and Z_T replaced by

$$Z_N(\zeta_e)\rightarrow Z'(\zeta_e), \tag{11}$$

$$Z_T(\zeta_e)\rightarrow-\frac{\zeta_e Z''(\zeta_e)}{2}, \tag{12}$$

where $Z(\zeta_e)$ is the usual plasma dispersion function[15] and primes denote derivatives with respect to its argument.

In arriving at the final system of equations it is useful to express the perpendicular components of the fluctuating electric and magnetic fields in terms of the parallel components. Using Eqs. (1), (3), and (4), yields

$$E_{1r}=\frac{ik_z}{k_0^2\epsilon_\perp-k_z^2}\frac{\partial}{\partial r}E_{1z}-\frac{k_0k_\theta}{k_0^2\epsilon_\perp-k_z^2}B_{1z}, \tag{13}$$

$$E_{1\theta}=\frac{-k_zk_\theta}{k_0^2\epsilon_\perp-k_z^2}E_{1z}-\frac{ik_0}{k_0^2\epsilon_\perp-k_z^2}\frac{\partial}{\partial r}B_{1z}, \tag{14}$$

$$B_{1r}=\frac{k_0\epsilon_\perp k_\theta}{k_0^2\epsilon_\perp-k_z^2}E_{1z}+\frac{ik_z}{k_0^2\epsilon_\perp-k_z^2}\frac{\partial}{\partial r}B_{1z}, \tag{15}$$

$$B_{1\theta}=\frac{ik_0\epsilon_\perp}{k_0^2\epsilon_\perp-k_z^2}\frac{\partial}{\partial r}E_{1z}-\frac{k_zk_\theta}{k_0^2\epsilon_\perp-k_z^2}B_{1z}, \tag{16}$$

where $k_\theta=m/r$ and $\epsilon_\perp=1+\omega_{pi}^2/\Omega_i^2$ is the perpendicular cold plasma dielectric in the limit $\omega\ll\Omega_i$.

Using Eqs. (13)–(16), and Eq. (8) in the parallel components of Eqs. (1) and (3) results in the system of eigenvalue equations governing the coupled electromagnetic fields E_{1z} and B_{1z},

$$\frac{1}{r}\frac{\partial}{\partial r}\left(\frac{r\epsilon_\perp}{k_0^2\epsilon_\perp-k_z^2}\frac{\partial}{\partial r}E_{1z}\right)+\left[\epsilon_\parallel-\frac{k_\theta^2\epsilon_\perp}{k_0^2\epsilon_\perp-k_z^2}-\left(\frac{\omega_{pe}}{k_z\overline{v}_e}\right)^2\frac{\omega_*}{\omega}\right]\times E_{1z}=-ig(r,\omega)B_{1z}, \tag{17}$$

$$\frac{1}{r}\frac{\partial}{\partial r}\left(\frac{r}{k_0^2\epsilon_\perp-k_z^2}\frac{\partial}{\partial r}B_{1z}\right)+\left[1-\frac{k_\theta^2}{k_0^2\epsilon_\perp-k_z^2}\right]B_{1z}=ig(r,\omega)E_{1z}, \tag{18}$$

where the function

$$g(r,\omega)=\frac{k_zk_\theta}{k_0}\frac{\partial}{\partial r}\left(\frac{1}{k_0^2\epsilon_\perp-k_z^2}\right), \tag{19}$$

characterizes the coupling of E_{1z} and B_{1z} through the density gradient, and

$$\epsilon_\parallel=1-\frac{\omega_{pi}^2}{\omega^2}-\frac{\omega_{pe}^2}{\omega^2}\zeta_e^2 Z_N(\zeta_e,\overline{\nu}). \tag{20}$$

Equations (17) and (18) describe the electromagnetic fields associated with drift-Alfvén waves. This becomes evident by considering the extreme electrostatic and electromagnetic limits. The electrostatic limit is obtained from Eq. (17) by neglecting B_{1z} and assuming $\omega\ll k_zv_A$ and $E_{1z}=-ik_z\phi_1$. Here, $v_A=c\Omega_i/\omega_{pi}$ is the Alfvén speed, and ϕ is the electrostatic potential. In this limit, Eq. (17) describes the potential associated with electrostatic drift waves and corresponds to the equation investigated in a previous publication.[16] The extreme electromagnetic limit is obtained by taking $\omega_*=0$ (i.e., uniform plasma). In this case Eqs. (17) and (18), respectively, describe the propagation of shear and compressional Alfvén waves. Hence, when the drift and Alfvén frequencies become comparable, i.e., $\mathrm{Re}(\omega_*)\simeq k_zv_A$, Eq. (17) describes the coupling of drift and shear-Alfvén waves while Eq. (18) describes the associated compressional fluctuation driven by the gradient in density.

The field formulation presented here describes the exact linear, low frequency electromagnetic response since the fast compressional Alfvén wave is explicitly included. However, for drift-Alfvén waves in plasmas characterized by $\overline{\beta}=2\overline{v}_e^2/v_A^2\ll M/m_e$, it is common to formulate the problem in

terms of vector and scalar potentials.[17] The potential formulation involves expressing the wave fields in terms of the electrostatic potential ϕ_1 and the vector potential $\mathbf{A}_1$ under the assumption that the perpendicular electric field is electrostatic. Consequently, the perpendicular components of $\mathbf{A}_1$ are zero and the compressional mode is eliminated.[18] For completeness, the alternative potential formulation of this problem is given in Appendix B.

III. LOCAL ANALYSIS

Before proceeding with the numerical solution of Eqs. (17) and (18), it is useful to identify the various modes predicted by a local analysis. The local dispersion relation, obtained by neglecting the radial derivatives of the wave fields in Eqs. (17) and (18) as well as the ion contribution and unity in $\epsilon_\parallel$ and unity in $\epsilon_\perp$, can be written as

$$\left\{\frac{K_\perp^2\overline{\beta}}{2}+(w^2-1)\left[\frac{w_*}{w}+\frac{1}{2}Z_N\left(\frac{w}{\sqrt{\overline{\beta}}}\right)\right]\right\}\{K_\perp^2+K_z^2(1-w^2)\}$$
$$=\frac{K_\perp^2\overline{\beta}}{2w^2}\left[\frac{\partial}{\partial\rho}\ln\left(\frac{1}{w^2-1}\right)\right]^2, \tag{21}$$

where

$$w_*=\frac{\omega_*}{k_z v_A}=\frac{\overline{\beta}\chi}{4}(Z_N\partial_\rho\ln N+Z_T\partial_\rho\ln T). \tag{22}$$

The various scaled quantities are $w=\omega/k_z v_A$, $\chi=(k_\perp/k_z)\sqrt{m/M}$, $K_\perp=(m/r)\delta$, $K_z=k_z\delta$, $\overline{\beta}=2\overline{v_e^2}/v_A^2$, $\rho=r/\delta$, and $\delta=c/\omega_{pe}$. Terms within the left set of braces on the left side of Eq. (21) are associated with drift and shear-Alfvén modes, while terms in the right set of braces result directly from the inclusion of finite B_{1z} and are associated with compressional Alfvén modes (i.e., $w^2=1+K_\perp^2/K_z^2$). The term on the right side of Eq. (21) is proportional to the square of the density gradient and determines the coupling between the drift-Alfvén and the compressional Alfvén modes. Note that the coupling term does not contain any contribution from the temperature gradient.

Because of the relative complexity, for a given set of wave numbers and plasma parameters, Eq. (21) must be solved numerically for w. However, simple analytic expressions which approximate the roots of Eq. (21) in the $\overline{\beta}\gg 1$ and $\overline{\beta}\ll 1$ limits can be obtained using the collisionless model. In this Section, we investigate the effects of density and temperature gradients separately to clearly distinguish instabilities associated with each type of striation. Furthermore, we assume that $K_\perp$, χ, and the scaled density and temperature gradient scale lengths are of order unity. All wave numbers are considered to be positive real quantities and w is complex.

A. Density gradient modes

First, we investigate Alfvénic modes ($w\approx 1$) associated with a pure density gradient ($\partial_r n_0>0$). In the $\overline{\beta}\ll 1$ limit, we approximate $Z_N\approx\overline{\beta}/w^2$ in Eq. (21) and neglect w_*/w compared with $Z_N/2$, and $K_z^2(1-w^2)$ compared with $K_\perp^2$. With these approximations, Eq. (21) reduces to

$$(w^2-1)^3+K_\perp^2 w^2(w^2-1)^2-w^4(\partial_\rho\ln N)^2=0. \tag{23}$$

Note that when $\partial_\rho\ln N=0$, the usual dispersion relation for the inertial Alfvén wave, $w^2=(1+K_\perp^2)^{-1}$, is recovered. To solve for w in the presence of a finite density gradient we let

$$w\simeq\pm(1+\delta w), \tag{24}$$

in Eq. (23) and, assuming $|\delta w|\ll 1$, neglect terms of order δw^2 compared with unity. Solving for δw then yields the instability condition

$$\partial_\rho\ln N(\rho)>\frac{2}{3\sqrt{3}}K_\perp^3. \tag{25}$$

When this condition is satisfied, there are three solutions for δw. One solution is purely real and the other two are complex conjugates.

For Alfvén modes in the $\overline{\beta}\gg 1$ limit, we expand Z_N for small argument ($Z_N\approx -2$). Note that if $w_*=0$, the usual dispersion relation for the kinetic Alfvén wave, i.e., $W^2=1+K_\perp^2\overline{\beta}/2$, is recovered from Eq. (21). For a density gradient with a scale length on the order of c/ω_{pe}, we can neglect $Z_N/2$ compared with w_*/w and Eq. (21) reduces to

$$(w^2-1)^3\chi\partial_\rho\ln N-w(w^2-1)^2K_\perp^2+w^3(\partial_\rho\ln N)^2=0. \tag{26}$$

Substituting Eq. (24) into Eq. (26) and solving for δw then leads to the instability condition

$$\partial_\rho\ln N(\rho)>\left(\frac{4K_\perp^6}{27\chi^2}\right)^{(1/4)}. \tag{27}$$

When Eq. (27) is satisfied, there are again three distinct solutions for δw, one of which is purely real and two of which are complex conjugates. Hence, in both the low and high $\overline{\beta}$ regimes, a density gradient with a scale length satisfying Eqs. (25) and (27) is associated with three Alfvénic modes with $\mathrm{Re}\,\omega>0$ and three with $\mathrm{Re}\,\omega<0$. Of the three modes with either positive or negative ω, at least one is predicted to be unstable in either the $\overline{\beta}\gg 1$ or $\overline{\beta}\ll 1$ limits.

Next, we consider the drift wave solutions predicted by Eq. (21). We assume $\overline{\beta}\ll 1$ and $w\simeq w_*\ll 1$. In this limit, the term on the right side of Eq. (21) is negligible since it is of order $\overline{\beta}^3$ and Z_N can be expanded for small argument (i.e., $Z_N\approx -2$). With these approximations the real part of the frequency is,

$$\mathrm{Re}\,w\simeq-\frac{\overline{\beta}\chi}{2}\partial_\rho\ln N\left(1+\frac{K_\perp^2\overline{\beta}}{2}\right)^{-1}. \tag{28}$$

The growth rate is obtained by retaining the imaginary part of Z_N in w_* and evaluating it at $\zeta_{e0}=\mathrm{Re}\,w/\sqrt{\overline{\beta}}$, i.e.,

$$\mathrm{Im}(w)\simeq-\frac{\mathrm{Re}\,w}{2}\,\mathrm{Im}\,Z_N(\zeta_{e0}). \tag{29}$$

Note that $\mathrm{Im}\,w>0$ regardless of the sign of $\partial_r n_0$. Hence, the drift mode is always destabilized by the Landau resonance in the $\overline{\beta}\ll 1$ limit.

We now solve Eq. (21) numerically for w using wave numbers, density gradient scale lengths, and mass ratios typical of the LAPD density striation experiments ($K_\perp = 0.23$, $K_z = 10^{-3}$, $\partial_\rho \ln N = 0.35$, $M/M_p = 4$, where M_p is the proton mass); for simplicity we consider only the collisionless model. Figure 1 shows the dependence of the scaled frequency and scaled growth rate on $\bar{\beta}$ for the various roots ($\bar{\beta}$ is varied by changing B_0 and holding other parameters constant). In the $\bar{\beta} \gg 1$ regime there are three roots with real frequencies near $\omega = +k_z v_A$ (curves 1,2,3) and three near $\omega = -k_z v_A$ (curves 4,5,6). Modes with $\mathrm{Im}\, w > 0$ are unstable. The drift wave solution (curve 7) is damped (i.e., $\mathrm{Im}\, \omega < 0$) for $\bar{\beta} > 6$. In the $\bar{\beta} \ll 1$ regime there are also three roots with real frequencies near $\omega = +k_z v_A$ (curves 1,2,3) and three near $\omega = -k_z v_A$ (curves 5,6,7). In this regime, the drift wave solution (curve 4) becomes unstable. These characteristics are consistent with the approximate analytic analysis described earlier. It is noteworthy that two of the Alfvénic roots (1,3) are unstable for all $\bar{\beta}$. Although not shown in Fig. 1, the compressional modes predicted by Eq. (21) are stable and much higher in frequency than the shear Alfvén modes.

B. Temperature gradient modes

Next, we consider local Alfvénic instabilities associated with a temperature gradient. Note that setting $\partial_r n_0 = 0$ in Eq. (21) eliminates the coupling between shear and compressional modes and reduces the dispersion relation for the shear Alfvén modes to

$$\frac{K_\perp^2 \bar{\beta}}{2} + (w^2 - 1)\left[\frac{w_*}{w} + \frac{1}{2} Z_N\left(\frac{w}{\sqrt{\bar{\beta}}}\right)\right] = 0. \tag{30}$$

Analytic expressions for w can be obtained from the collisionless model by expanding w according to Eq. (24) in Eq. (30) and solving for δw. Assuming $|\delta w| \ll 1$ yields

$$\delta w \simeq -\frac{K_\perp^2 \bar{\beta}}{4}\left[\pm w_* + \frac{1}{2} Z_N\left(\pm\frac{1}{\sqrt{\bar{\beta}}}\right)\right]^{-1}, \tag{31}$$

where the function Z_T contained in w_* is also evaluated at $\zeta_e = \pm 1/\sqrt{\bar{\beta}}$. Here, the $\pm$ sign corresponds to the sign chosen for w in Eq. (24).

In the $\bar{\beta} \ll 1$ limit, $Z_N \approx Z_T \approx \bar{\beta}$, and $w_* \ll 1$. Using these approximations in Eq. (31) yields

$$\mathrm{Re}\, \delta w \approx -\frac{K_\perp^2}{2}\left[1 \mp \frac{\bar{\beta}\chi}{2}\partial_\rho \ln T\right], \tag{32}$$

$$\mathrm{Im}\, \delta w \approx \frac{K_\perp^2 \chi}{4}\, \mathrm{Im}\, Z_T(\pm 1/\sqrt{\bar{\beta}})\, \partial_\rho \ln T. \tag{33}$$

For $\partial_\rho \ln T < 0$, Eq. (33) indicates that the $w < 0$ solution is damped while the $w > 0$ solution is unstable.

We now solve Eq. (30) numerically for the mode approximately described by Eqs. (32) and (33). The dependence of the scaled frequency and scaled growth rate on $\bar{\beta}$ (obtained by varying B_0 as before) for different values of K_z is shown in Fig. 2. The solution corresponding to the $w < 0$

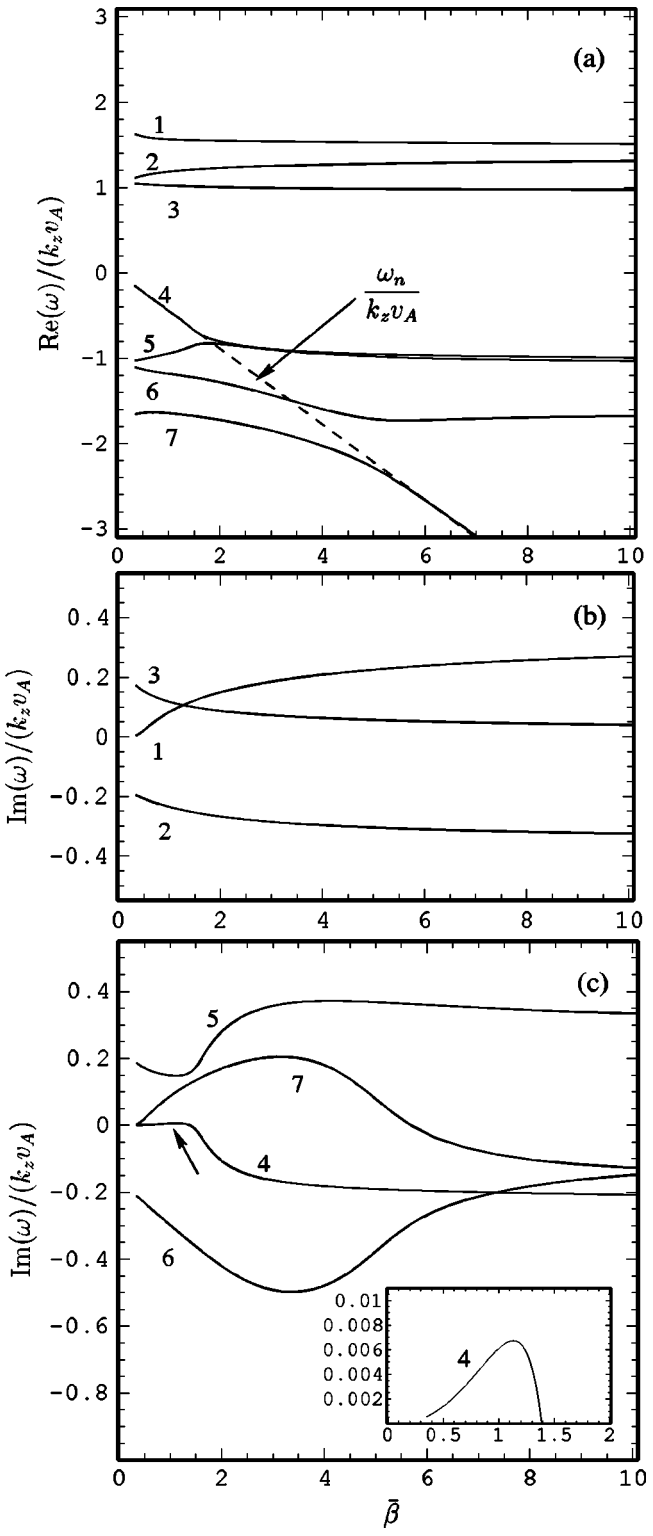

FIG. 1. Dependence of scaled frequency (a) and growth rate (b) and (c) on scaled beta, $\bar{\beta}$, for seven modes predicted by the local dispersion relation [Eq. (21)] for a pure density gradient ($\partial_r n_0 > 0$, $\partial_r T_e = 0$) for the collisionless model. Parameters are typical of a radial position within a density striation in the LAPD experiments. Dashed line in (a) corresponds to the scaled value of the electron fluid diamagnetic frequency, $\omega_n = -k_\theta c_s^2 \partial_r \ln n_0/\Omega_i$. Modes 4–7 propagate in the direction of the electron diamagnetic drift, while modes 1–3 propagate in the opposite direction. Growing modes have $\mathrm{Im}\, \omega > 0$. $\bar{\beta}$ is varied by changing the magnetic field strength while holding T_e, n_0, and $\partial_r n_0$ constant. Inset in panel (c) shows the growth rate of mode 4 in the region indicated by the arrow.

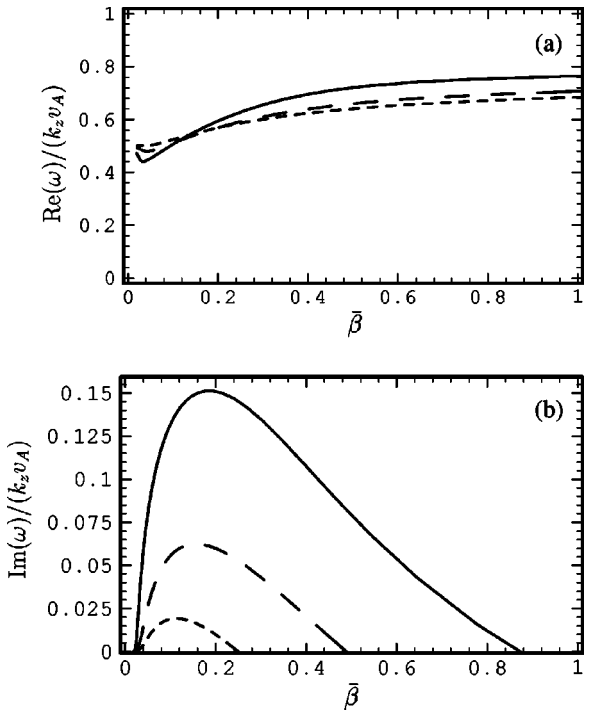

FIG. 2. Dependence of scaled frequency (a) and growth rate (b) on scaled beta, $\bar{\beta}$, predicted by the local dispersion relation [Eq. (21)] for a pure temperature gradient ($\partial_r n_0 = 0$, $\partial_r T_e < 0$) for the collisionless model. The curves correspond to different parallel wave numbers $k_z L_z/2\pi = 0.5$ (solid curve), 0.77 (larger dashed curve), 1.0 (small dashed curve). Parameters are typical of a radial position within a temperature striation in the LAPD experiments. All of these modes are unstable. $\bar{\beta}$ is varied by changing the magnetic field strength alone.

branch is damped and is not shown. These results are the predictions of the collisionless model using $\partial_\rho \ln T = -1.67$ and $K_\perp = 1.7$ which are characteristic of the LAPD experiments.[12] It is seen from Fig. 2 that the scaled frequency of the unstable mode is lower than the Alfvén frequency (i.e., $k_z v_A$) because of finite $K_\perp$ and is not very sensitive to K_z. The dependence of the frequency on $\bar{\beta}$ agrees with the trend predicted by Eq. (32). Modes with larger K_z tend to have smaller growth rates although the qualitative dependence of the growth rate on $\bar{\beta}$ is the same for the different K_z modes. The scaled growth rate is maximum near $\bar{\beta} \approx 0.1$. The growth rate decreases as $\bar{\beta}$ increases further and the mode with the largest growth rate is damped when $\bar{\beta} \approx 0.9$.

IV. EIGENMODE ANALYSIS

Next, we examine the eigenmodes obtained from numerically solving Eqs. (17) and (18). Eigenfunctions and complex eigenfrequencies are obtained using a numerical shooting method.[19] Equations (17) and (18) are integrated numerically from radii, r_0, near the center of a prescribed striation, and r_∞, far outside the striation, toward an interior radius, r_1, where the values and radial derivatives of E_{1z} and B_{1z} are required to be continuous. The numerical scheme requires the values of E_{1z} and B_{1z} and their radial derivatives to be specified at r_0 and r_∞. These are obtained by analytically solving Eqs. (17) and (18) in the asymptotic limits $r \to (0, \infty)$ and requiring that both E_{1z} and B_{1z} be finite as $r \to 0$, and evanescent as $r \to \infty$.

The asymptotic solutions of Eqs. (17) and (18) satisfying the boundary conditions are

$$\psi_{1z}(r \to \infty) \to C_\psi H_m^{\pm}(k_\psi r) \approx C_\psi \sqrt{2/(\pi k_\psi r)}\, \exp\left[\pm i \left(k_\psi r - \frac{\pi}{2} m - \frac{\pi}{4} \right) \right], \tag{34}$$

$$\psi_{1z}(r \to 0) \to D_\psi J_m(K_\psi r) \approx D_\psi \frac{(K_\psi r/2)^m}{\Gamma(m+1)}, \tag{35}$$

where Γ is the gamma function, and J_m, $H_m^+ = H_m^{(1)}$, and $H_m^- = H_m^{(2)}$ are the usual Bessel and Hankel functions of order m. Symbolically, ψ_{1z} is either E_{1z} or B_{1z} and

$$k_E = \frac{\epsilon_\parallel}{\epsilon_\perp}(k_0^2 \epsilon_\perp - k_z^2)\big|_{r=\infty}, \tag{36}$$

$$k_B = (k_0^2 \epsilon_\perp - k_z^2)\big|_{r=\infty}, \tag{37}$$

$$K_E = \frac{\epsilon_\parallel}{\epsilon_\perp}(k_0^2 \epsilon_\perp - k_z^2)\big|_{r=0}, \tag{38}$$

$$K_B = (k_0^2 \epsilon_\perp - k_z^2)\big|_{r=0}. \tag{39}$$

The ($\pm$) sign in Eq. (34) must be chosen such that, for a given ω, ψ_{1z} is evanescent as $r \to \infty$. The four quantities C_ψ, D_ψ are complex constants which are to be determined along with ω. We normalize the solution by choosing $C_E = 1$ and provide initial trial values for $\{C_B, D_E, D_B, \omega\}$ to start the numerical process. Equations (17) and (18) are then integrated from the boundaries to r_1 and the trial values are iteratively corrected until E_{1z}, B_{1z}, and their radial derivatives are continuous at r_1.

For the sake of clarity, we first investigate the eigenmodes of density striations ($\partial_r n_0 > 0$, $\partial_r T_e = 0$) and temperature striations ($\partial_r n_0 = 0$, $\partial_r T_e < 0$) separately. Later, when comparing the results with LAPD experiments, we allow for both gradients to be present.

A. Density striations

For a pure density striation, the scaled background plasma density is described analytically by

$$N(r) = 1 - \delta_N \exp(-r^4/L_N^4). \tag{40}$$

This functional form is chosen because it reasonably fits the shape of density striations created in the LAPD experiments for $\delta_N = 0.71$ and $L_N = 1.6$ cm. The density outside the striation is chosen to be $n_0 = 2.6 \times 10^{12}\ \mathrm{cm}^{-3}$. A uniform electron temperature, $T_e = 11.6$ eV, is assumed. This value is typical of the background plasma in the previously published LAPD experiments.[12]

Figure 3 shows the dependence of the frequencies and growth rates (scaled to the ion gyrofrequency) of three fundamental eigenmodes ($h = 1$, $m = 1$, $k_z L_z = \pi$) on magnetic field B_0 predicted by the collisionless form of Eqs. (17) and (18). Here, h labels the radial mode number. The dashed lines in Fig. 3(a) bracket the range of Alfvén frequencies associated with the density striation. For $B_0 > 2$ kG, modes 1

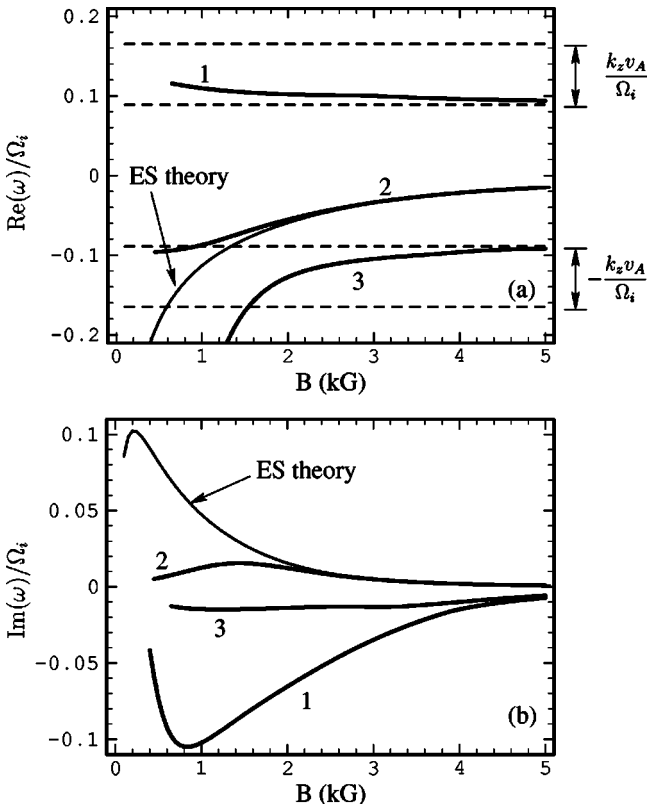

FIG. 3. Dependence on magnetic field of the frequency (a) and growth rate (b) [scaled to the ion cyclotron frequency] of three different modes (1–3) obtained from the numerical solution of the full electromagnetic theory [Eqs. (17) and (18)] for a pure density striation ($\partial_r n_0 > 0$, $\partial_r T_e = 0$) using the collisionless model. Modes correspond to the fundamental ($h=1$, $m=1$, $k_z L_z = \pi$). Thin curves indicate the prediction of pure electrostatic theory. Dashed lines bracket the range of Alfvénic frequencies associated with the striation for this value of k_z. Parameters are typical of density striations in LAPD experiments.

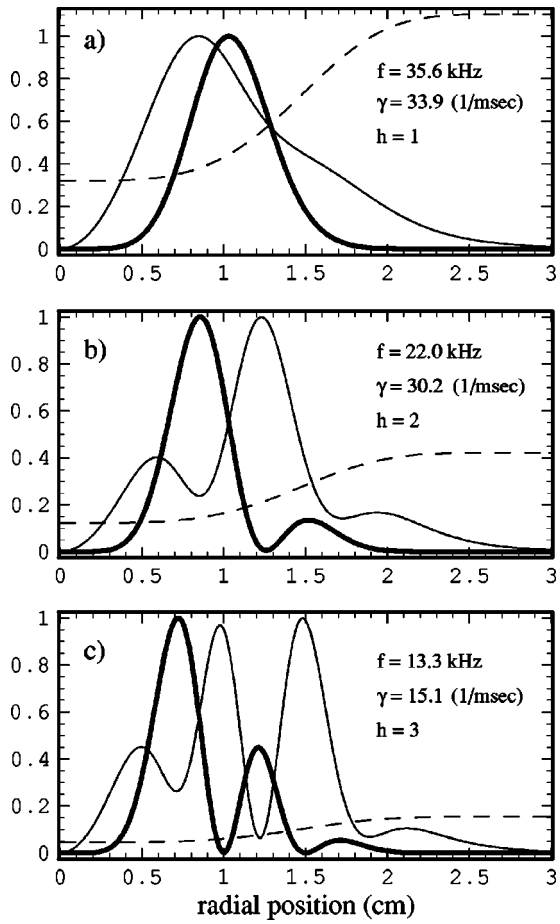

FIG. 4. Radial dependence of density (actually $|n_{1i}|^2$, thick curve) and magnetic ($|\mathbf{B}_1|$, thin curve) eigenfunctions associated with the unstable mode labeled 2 in Fig. 3, for $B_0 = 1$ kG. Eigenvalues and radial mode number are shown in each panel. Dashed curve corresponds to local value of $[\mathrm{Re}\,\omega/(k_z v_A)]^2$.

and 3 represent damped Alfvénic fluctuations while mode 2 is an unstable drift-wave eigenmode. As B_0 decreases to below 1 kG, the unstable mode 2 becomes an Alfvénic eigenmode while the real frequency of mode 3 approaches the electron diamagnetic drift frequency. The thin curves in Fig. 3 labeled ES correspond to the eigenmode predicted by purely electrostatic (ES) theory.

Recall that the local analysis of Sec. III predicts six distinct roots with frequencies near the local Alfvén frequency while only three modes satisfying the boundary conditions were found in the integration of Eqs. (17) and (18). However, the global analysis is inherently different from the local analysis in that the density striation is associated with a continuous range of Alfvén frequencies and the two Alfvénic eigenmodes in Fig. 3 result from a self-consistent averaging over the profile including the Alfvén resonances in the derivative terms of Eqs. (17) and (18).

Note also that the frequency of mode 2 remains below the range of local Alfvén frequencies in the gradient region. Hence, for this mode, a local Alfvén resonance is self-consistently avoided. Although the other two modes (1 and 3) have frequencies which are within the range of local Alfvén frequencies, a large damping rate prevents any singularity associated with a local Alfvén resonance from becoming important.

As seen from Fig. 3, the electrostatic and electromagnetic theories predict a nearly identical frequency and growth rate for the unstable mode (2) in the region $B_0 > 2$ kG. This regime corresponds to $\overline{\beta} < 1$. As B_0 decreases to 1 kG, $\overline{\beta}$ approaches unity and electrostatic theory does not properly describe this mode. In comparison with electromagnetic theory, the electrostatic theory predicts a larger frequency and growth rate.

The radial dependence of the density (thick curve) and magnetic (thin curve) eigenfunctions corresponding to mode 2 with radial mode numbers $h = 1,2,3$ are shown in Fig. 4 for $B_0 = 1$ kG. The local values of $[|\mathrm{Re}(\omega)|/k_z v_A]^2$ (dashed curves) are also shown as an indication of the electromagnetic character of the mode. Essentially, modes with $[|\mathrm{Re}(\omega)|/k_z v_A]^2 \ll 1$ are more electrostatic in character. It is seen from Fig. 4 that only the fundamental eigenmode ($h = 1$) has a frequency large enough to require electromagnetic theory for a proper description. Higher order radial modes, which have progressively smaller values of $[\mathrm{Re}(\omega)/k_z v_A]^2$, have frequencies and growth rates that are well approximated by electrostatic theory. It is also seen that

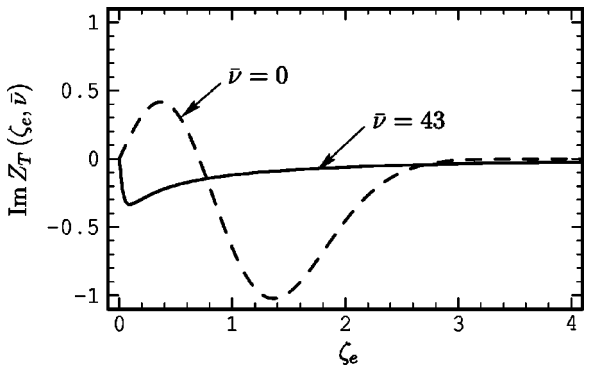

FIG. 5. Dependence of the imaginary part of the kinetic response function, $Z_T(\zeta_e,\bar{\nu})$, for a pure temperature gradient on scaled parallel phase velocity, ζ_e. Collisionless case corresponds to dashed curves ($\bar{\nu}=0$) while solid curve ($\bar{\nu}=43$) is more characteristic of actual conditions in the temperature striation experiment in the LAPD. Collisions allow the mode to be unstable at small $\bar{\beta}$ where the collisionless case is stable (i.e., Im $Z_T>0$).

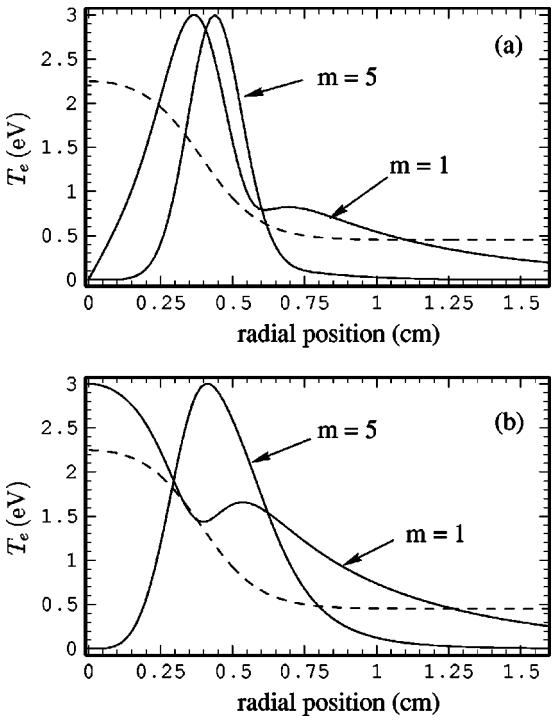

FIG. 6. Radial dependence of density ($|n_{1i}|$, (a)) and magnetic ($|\mathbf{B}_1|$, (b)) eigenfunctions for an unstable mode predicted by collisionless theory for a pure temperature striation ($\partial_r n_0=0$). Behavior for two different azimuthal modes is shown for the fundamental mode ($h=1$, $k_z L_z=\pi$). The dashed curve corresponds to the electron temperature profile. Eigenfunctions are in arbitrary units.

the magnetic eigenfunctions generally exhibit a broader radial extent than the density eigenfunctions and, for higher order radial modes, tend to peak further towards the outside of the striation. We also note that the magnetic eigenfunctions are predominantly shear waves, i.e., $|B_{1z}|/|\mathbf{B}_\perp| \approx 10^{-4}$. This is to be expected since $\bar{\beta} \ll M/m_e$.

B. Temperature striations

Next, we analyze the properties of drift-Alfvén eigenmodes associated with a pure temperature striation ($\partial_r T_e<0$, $\partial_r n_0=0$). A major simplification in this striation is that the shear and compressional Alfvén modes are decoupled. This is evident from Eqs. (17) and (18) since the function $g(r,\omega)$, which couples E_{1z} and B_{1z} is only proportional to the density gradient. Hence, in the subsequent discussions of pure temperature striations, the shear Alfvénic modes are obtained by solving only Eq. (17).

Here we emphasize the comparison between the predictions of the collisional and collisionless models since the plasma response to a temperature gradient changes significantly as the plasma becomes highly collisional. This behavior is illustrated in Fig. 5 where the dependence of Im Z_T on scaled phase velocity is shown for the collisionless case ($\bar{\nu}=0$) and for $\bar{\nu}=43$, which is more characteristic of the LAPD experiments. It is seen that a large collision frequency can change the sign of Im Z_T in the interval $\zeta_e<0.7$, and in fact, the peak value is shifted towards small ζ_e (≈ 0.2). Hence, Eq. (33) suggests that strong collisionality can have a destabilizing effect on modes having small ζ_e. Of course, since Eq. (33) is obtained for the collisionless case and with the assumption that $\bar{\beta} \ll 1$, a full numerical analysis is required to properly determine mode stability when $\bar{\beta} \geqslant 1$ and the collision frequency is large.

In the numerical study, the radial variation of the scaled temperature is represented by

$$T(r)=1+\delta_T\left[1+\frac{\sinh^2(r/L_T)}{\sinh^2(\Delta/L_T)}\right]^{-1}, \tag{41}$$

where the constants δ_T and L_T characterize the temperature increase above the background level ($\delta_T>0$) and the temperature gradient scale length, respectively. The quantity Δ corresponds to the radial position at which the temperature drops to half of its peak value. A temperature profile associated with $\delta_T=4.0$, $L_T=0.2$ cm, and $\Delta=0.4$ cm is shown in Fig. 6 (dashed curve). It is assumed that the electron temperature outside the striation is 0.45 eV (characteristic of afterglow plasma conditions) and that the plasma density is uniform ($n_0=1.5\times 10^{12}\,\mathrm{cm}^{-3}$). This analytic representation of a striation closely approximates the temperature striations created in the LAPD experiments[13] that use a narrow electron beam as a heat source.

The solid curves in Fig. 6 illustrate the radial dependence of the density [Fig. 6(a)] and magnetic [Fig. 6(b)] eigenfunctions for two unstable modes predicted by the collisionless model. The two eigenmodes shown correspond to different azimuthal mode numbers ($m=1,5$). It is seen that the amplitude of the density fluctuation peaks close to the location of the largest temperature gradient for both $m=1$ and 5, although the $m=5$ mode is slightly shifted towards the outside of the striation, as expected. The amplitude of the magnetic fluctuation for the $m=1$ mode is largest in the center of the striation in contrast to higher m-modes where the magnetic fluctuation peaks within the maximum gradient region and is zero at $r=0$.

The dependence of the eigenfrequency and growth rate on azimuthal mode number is shown in Fig. 7 for both collisionless and collisional models; the temperature profile is

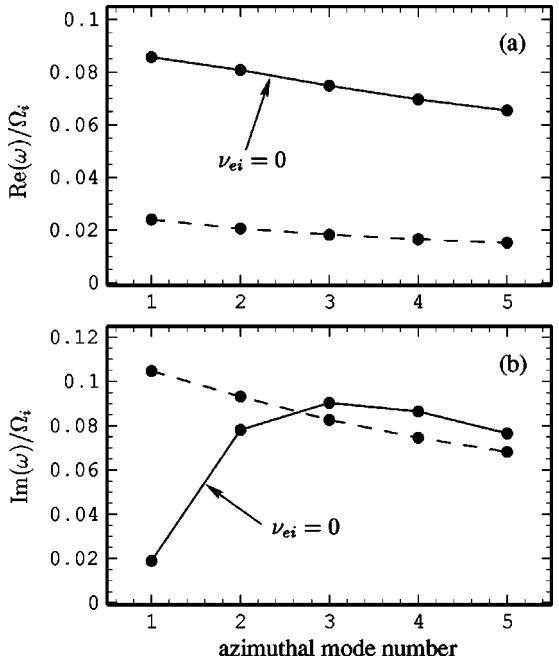

FIG. 7. Dependence of frequency (a) and growth rate (b) [scaled to the ion cyclotron frequency] on azimuthal mode number, m, for unstable modes in a pure temperature striation ($\partial_r n_0=0$, $\partial_r T_e<0$) predicted by the numerical solution of Eq. (17). Predictions of collisional and collisionless theory are indicated by dashed and solid curves, respectively. Mode corresponds to $h=1$, $k_z L_z=\pi$. The temperature profile is shown in Fig. 6. Parameters are typical of LAPD experiments.

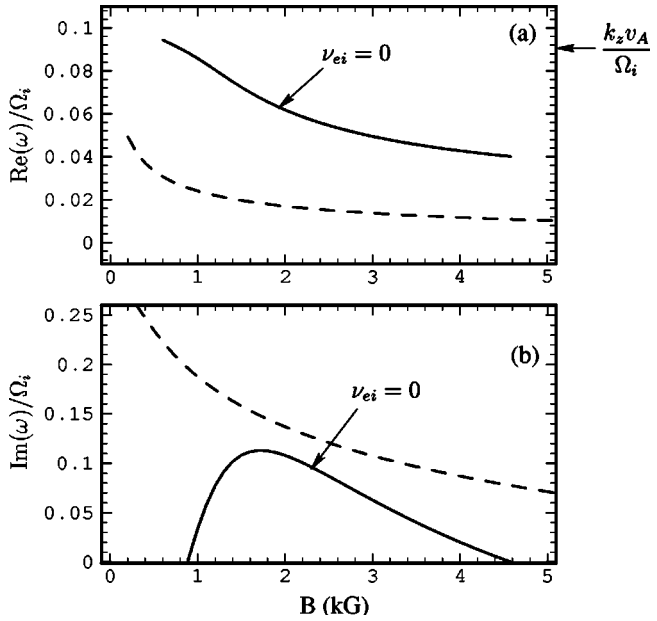

FIG. 8. Dependence of frequency (a) and growth rate (b) [scaled to the ion cyclotron frequency] on magnetic field strength for an unstable mode in a pure temperature striation ($\partial_r n_0=0$, $\partial_r T_e<0$) predicted by the numerical solution of Eq. (17). Predictions of collisional and collisionless theory are indicated by dashed and solid curves, respectively. Mode corresponds to $h=1$, $m=1$, $k_z L_z=\pi$. The temperature profile is shown in Fig. 6 and is held constant as B_0 changes. Parameters are typical of LAPD experiments.

as shown in Fig. 6. It is seen that the mode frequency does not depend strongly on m for either the collisionless or collisional model, however, the frequency for the collisional case is significantly smaller. Another difference is that the collisionless model predicts that the growth rate of the $m=1$ mode is smaller than that of larger m-modes, while in the collisional model the fastest growing mode has $m=1$.

Figure 8 shows the dependence of the frequency and the growth rate on the strength of the confining magnetic field for the $m=1$ eigenmode in Fig. 7. The frequency predicted by the collisionless model is close to the Alfvén frequency at $B_0=1$ kG (as indicated by the arrow) and decreases as B_0 increases. The collisional model predicts a similar trend although the frequency is roughly a factor of 3 smaller. In the collisionless model the mode is unstable in the range $1\,\mathrm{kG}<B_0<4.5\,\mathrm{kG}$, while for the collisional model, the growth rate is larger and the mode is unstable over the entire range of B_0 shown.

V. COMPARISON WITH EXPERIMENTS

Next we compare the theoretical predictions with the results of the LAPD pressure[12] and temperature[13] striation experiments. The ion species considered is singly ionized Helium, as is appropriate to the experiments. Also note that in the experiments the ion temperature ranges from 0.1 to 1 eV while the present model considers zero temperature ions. Only the collisional model is used when making direct comparisons with experimental data.

A. Pressure striation experiment

To accurately model the pressure striation in the LAPD experiment,[12] the radial density profile is represented by Eq. (40) while the scaled temperature is given a similar functional form, i.e.,

$$T(r)=1-\delta_T\exp(-r^4/L_T^4). \tag{42}$$

The constants which characterize the density and temperature profiles are chosen to be $\delta_N=0.71$, $L_N=1.6\,\mathrm{cm}$, $\delta_T=0.45$, and $L_T=1.14\,\mathrm{cm}$. Outside the striation, $n_0=2.6\times10^{12}\,\mathrm{cm}^{-3}$ and $T_e=11.6\,\mathrm{eV}$. With these parameter choices, the analytical density and temperature profiles approximate closely the measured profiles (shown later in Fig. 11).

Figure 9 shows the dependence of the frequency and the growth rate on k_z predicted by the electromagnetic and the electrostatic theories for the collisional model. The electromagnetic mode shown in the figure is the collisional counterpart of mode 2 in Fig. 3. It is seen that the electrostatic and electromagnetic predictions are similar for larger k_z but differ somewhat for smaller k_z. While the growth rate of the electrostatic model is largest when $k_z L_z=\pi$ (i.e., the longest parallel wavelength allowed in the device for a standing wave), the electromagnetic growth rate is smaller and relatively insensitive to k_z when $k_z L_z<1.5$. The frequency for the electrostatic model at $k_z L_z=\pi$ is very close to the frequency of the largest density fluctuation observed in the experiment ($\simeq$37 kHz) and slightly larger than the value predicted by the full electromagnetic theory. The frequency predicted by the electromagnetic theory increases with k_z and is closer to the frequency in the experiment when $k_z L_z=2\pi$. However, it is unlikely that the fluctuations in the

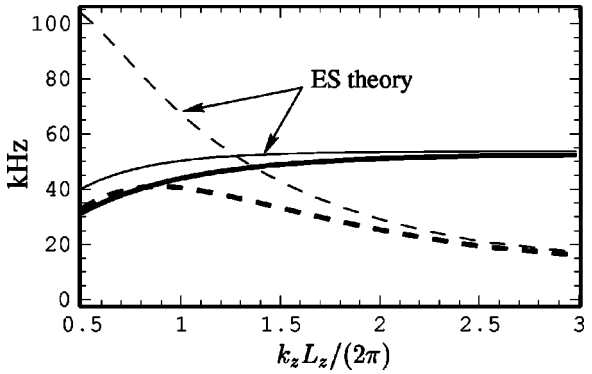

FIG. 9. Comparison between predictions of electrostatic theory and full electromagnetic theory for the collisionless model. Shown is the dependence of the frequency (solid curves) and growth rate (dashed curves) on parallel wave number for the numerical solutions of the eigenvalue problem associated with a striation having the density and temperature profiles shown in Fig. 11. Here $h=1$, $m=1$, and $B_0=1$ kG. Electromagnetic results are the thicker curves.

experiment have an axial wave numbers this large since the measured spectrum of density fluctuations is identical over half the length of the device. However, no detailed measurement of k_z has been made in the experiments.

Figure 10 displays the frequencies of various unstable electromagnetic eigenmodes with $k_z L_z=\pi$ but having different azimuthal and radial mode numbers. Note that since the frequencies of the different azimuthal modes with the same radial mode number are close to each other, the peaks seen in the measured spectrum may actually consist of a superposition of several eigenmodes with different azimuthal mode numbers. The separation in frequency between the different radial eigenmodes is comparable to the frequency separation of the three largest density fluctuations observed in the experiment (indicated by the arrows). However, if the peaks in the measured spectrum are interpreted as arising mainly from different radial eigenmodes, then the theoretically predicted frequencies of the $h=1,2,3$ modes are systematically lower than the observed fluctuations at 37, 25, and 18 kHz by about 5 kHz. This discrepancy may be caused by the Doppler shift

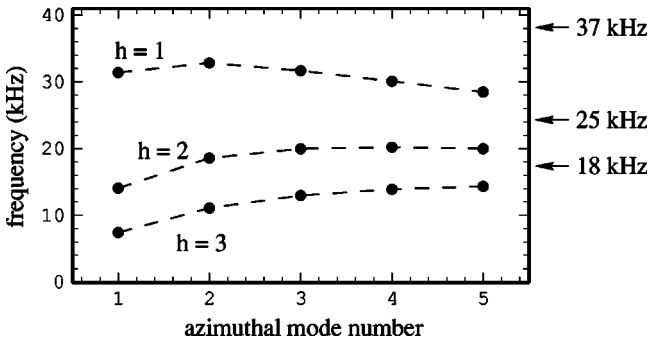

FIG. 10. Dependence of the theoretically predicted eigenfrequencies of unstable modes (heavy dots) on azimuthal mode number. The arrows correspond to the frequency of the dominant spectral peaks observed in the pressure striation experiment in the LAPD [e.g., Fig. 9 of Ref. 12] having the density and temperature profiles shown in Fig. 11 and $B_0=1$ kG. Theory corresponds to the full electromagnetic description [Eqs. (17) and (18)] including collisions. Dashed lines connect frequencies having the same radial mode number.

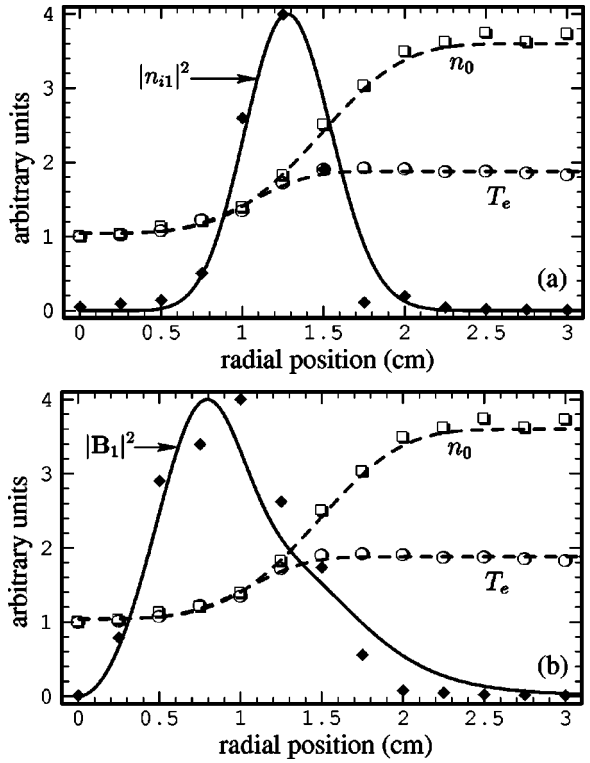

FIG. 11. Comparison of eigenfunctions measured in LAPD experiments to predictions of full electromagnetic theory including collisions. Open squares and circles are measured values of density and temperature profiles scaled to their value at $r=0$. Dashed curves are analytical fits used in eigenvalue calculation. Solid curves correspond to the square of the density fluctuation (a) and the square of the magnetic fluctuation (b) predicted by theory for $m=2$, $k_z L_z=\pi$. Diamonds correspond to scaled experimental measurements. $B_0=1$ kG.

associated with the azimuthal rotation of the plasma by a radial electric field. If so, then a field on the order of 10 V/m pointing radially outward would account for the 5 kHz difference. While such a field could possibly exist in the device, a more detailed theoretical and experimental investigation of this issue is needed.

The next comparison tests the radial profiles of the density and magnetic eigenfunctions associated with the 37 kHz fluctuation observed in the experiment. We compare the experimental measurements with the fastest growing eigenmode predicted by theory, i.e., the $h=1$, $m=2$, $k_z L_z=\pi$ mode in Fig. 10. The frequency of this mode ($\simeq$33 kHz) is close to the experimental value. The open symbols shown in Fig. 11 denote experimental measurements of the scaled radial profiles of density and electron temperature; the dashed curves passing through these symbols are the analytic fits obtained from Eqs. (40) and (42) used in solving Eqs. (17) and (18). The solid curve shown in Fig. 11(a) is the theoretical prediction for the radial dependence of the density fluctuation (actually, $|n_{1i}|^2$). The solid diamonds represent the fluctuations in ion saturation current measured using a small Langmuir probe. The solid curve in Fig. 11(b) displays the radial dependence of the theoretical magnetic fluctuation (i.e., $|\mathbf{B}_1|^2$) while the solid diamonds are the measured values (in arbitrary units) obtained with a small magnetic induction loop. It is found that the predicted shape of the density and

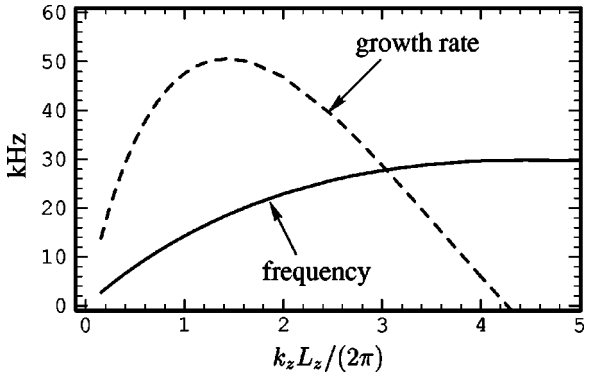

FIG. 12. Dependence of the frequency and growth rate on parallel wave number predicted by the full electromagnetic theory with collisions for a pure temperature striation ($\partial_r n_0 = 0$). Here, $B_0 = 1$ kG, $m = 1$, $h = 1$. The temperature profile is shown in Fig. 6.

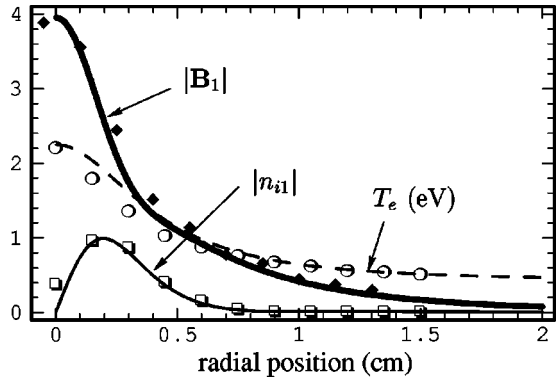

FIG. 13. Comparison of measured and theoretically predicted radial eigenfunctions associated with a pure temperature striation ($\partial_r n_0 = 0$). Symbols correspond to measured quantities in the LAPD experiment and solid curves are theoretical predictions. Dashed curve is the theoretical fit to measured temperature profile used in the eigenvalue calculation. Heavy solid curve corresponds to the predicted magnetic eigenfunction and the thin solid curve to the corresponding density eigenfunction. Here, $m = 1$, $h = 1$, $k_z L_z = 5\pi$, $B_0 = 1$ kG. Eigenfunctions are in arbitrary units. Theoretical results are the prediction of the full electromagnetic model with collisions. The theoretically predicted eigenfrequency is 26 kHz and the experimentally observed value is 38 kHz.

magnetic eigenfunctions are in good agreement with the observations.

B. Temperature striation experiment

We model the radial profile of the temperature striation using Eq. (41) with $\delta_T = 4.0$, $L_T = 0.2$ cm, and $\Delta = 0.4$ cm. It should be noted that in this heat transport-related experiment[13] there is more uncertainty in the parallel wavelength of the fluctuation than in the pressure striation study because the axial extent of the pure temperature striation, which is determined simultaneously by axial and radial transport, is likely to be shorter than the device length and varies in time. Hence, assuming standing waves in the axial direction within the temperature striation, the value of k_z is not limited to integral multiples of $L_z/2$ as is expected in the pressure striation experiment. However, the largest wavelength possible is bounded by $k_z L_z = \pi$.

Figure 12 shows the predicted dependence of the frequency and the growth rate on parallel wave number for the collisional mode shown in Fig. 8. In this case the value of k_z can, in principle, vary continuously since the length of the temperature striation can also vary. It is seen that instability occurs for $k_z L_z < 8\pi$. Over the range of instability, the frequency increases with k_z from about 10 kHz at $k_z L_z = \pi$ to just below 30 kHz. For comparison, the dominant fluctuation observed in the experiment has a frequency of 37 kHz, which is above the range predicted by theory.

Lastly, we compare the radial profiles of the observed density and magnetic fluctuations with the theoretical predictions. The heavier solid curve in Fig. 13 represents the predicted magnetic eigenfunction (i.e., $|\mathbf{B}_1|$) while the solid diamonds correspond to experimental values (in arbitrary units) measured with a small magnetic induction loop. The predicted density eigenfunction (i.e., $|n_{i1}|$) is represented by the lighter solid curve. Open squares denote measurements of the fluctuating ion saturation current amplitude in arbitrary units. The theoretical eigenmode has $h = 1$, $m = 1$, $k_z L_z/2\pi = 2.5$. Although the predicted frequency of this mode (≈ 26 kHz) is somewhat low compared with the observed value, the predicted shape of the density and magnetic fluctuation agrees quite well with the experimental observations.

VI. CONCLUSIONS

This analytical and numerical study illustrates the properties and parameter dependences of the low frequency ($\omega \ll \Omega_i$) electromagnetic instabilities associated with narrow pressure striations (having transverse scale on the order of the electron skin-depth) embedded within a magnetized plasma and under conditions in which the ion response is appropriately described as that of a cold magnetized fluid. This is a generic situation encountered in plasmas that are far from thermal equilibrium and presently is a topic of interest to interpretations of spacecraft observations and laboratory experiments that probe the fundamentals of heat transport in magnetized plasmas.

A full electromagnetic formulation of the relevant linear eigenvalue problem is obtained in terms of the axial fields (E_z, B_z) commonly neglected in related studies based on the potential formulation (ϕ, A_z). The analysis naturally describes drift modes, shear Alfvén waves, compressional Alfvén waves, and ion acoustic modes, together with the couplings associated with gradients in density and temperature. In addition to the stability question specifically explored in this work, the formulation can be used as the starting point to investigate the scattering, direct conversion, and resonant mode conversion induced on the various modes by narrow pressure striations.

The present study focuses on the kinetic response of the electrons and incorporates the effect of velocity dependent pitch-angle collisions. This approach permits a comparison between the results of the idealized collisionless model and the collisional counterpart.

To concisely illustrate the various parameter dependences of the instabilities (radial, azimuthal, and axial mode numbers; strength of confining magnetic field) specific parameter choices are used that correspond to controlled pressure striations generated in the LAPD facility at the Univer-

sity of California, Los Angeles. The eigenmodes triggered by two different types of pressure striations are examined in detail. They consist of: (1) localized depletions in both density and electron temperature; (2) localized enhancements in electron temperature.

When comparing the results of the full electromagnetic theory with the predictions of a more limited, pure electrostatic formulation (but having similar kinetic electron response) it is found that in general the electromagnetic effects decrease the frequency [Fig. 3(a)] of the modes and significantly reduce the growth rate [Fig. 3(b)]. The self-consistent electromagnetic effects provide a self-avoidance of the local Alfvén resonance that would be predicted by the electrostatic theory to occur throughout the profile of a density depletion [Fig. 3(a)]. The electromagnetic corrections are shown to be unimportant for higher order radial modes (Fig. 4) and large values of the confining magnetic field (Fig. 3).

A feature of the electromagnetic eigenmodes excited in a pure temperature striation is that their frequency is insensitive to the azimuthal mode number for the collisionless and collisional models [Fig. 7(a)]. This behavior points out that the usual estimate based on the local diamagnetic frequency fails to properly describe these systems.

A significant difference exists between the collisionless and collisional models for the temperature striations generated in the LAPD experiments. At the fundamental level the differences can be traced to the topological changes in the temperature-gradient response function Z_T (Fig. 5) as the collision frequency is increased. The effect on the frequency of the eigenmodes is quite significant, i.e., a lowering by a factor of 4 results [Fig. 7(a)]. The other important change is that the collisional case prefers the growth of the $m=1$ mode, which in the collisionless model is substantially depressed [Fig. 7(b)]. The dominant $m=1$ mode in the collisional regime exhibits a larger growth rate than the collisionless counterpart over a wide range of values of the confining magnetic field [Fig. 8(b)]. Another important property of the collisional instability is that its growth rate is relatively insensitive to the parallel wave number (Fig. 9). This implies that in a slowly expanding heat plume (whose rate of expansion is determined by simultaneous radial and axial heat transport) the corresponding slow changes in k_z do not cause an abrupt onset or quenching of the instability.

When comparing the predicted frequency of the unstable eigenmodes supported in the pressure depletion with the experimentally observed values (Fig. 10) a systematic discrepancy of about 5 kHz is found. It is reasonable to speculate that the difference results from $E\times B$ rotation not included in the present formulation (but not difficult to incorporate), but no experimentally conclusive information on this point is presently available. Of course, in other drift-wave experiments[20,21] this effect has been shown to be quite prominent. It should also be mentioned that the ion diamagnetic frequency can be estimated to be on the order of a few kHz, a value in the range of the discrepancy. Since the present theory treats the ions as a cold fluid, the reader should be aware of its implications. It is noteworthy that the limited electrostatic theory gives a much closer agreement with the observations. In the case of the pure temperature striation the predicted frequency of the dominant $m=1$ mode (clearly identified in the experiment) is also smaller than the measured value.

The predicted radial structure of the density and magnetic fluctuations are found to be in excellent agreement with the experimental measurements in the pressure depletion (Fig. 11) as well as in the temperature striation (Fig. 13).

In conclusion, a general formulation of drift-Alfvén waves in narrow pressure striations has been presented that is capable of describing detailed observations in controlled laboratory experiments. From this comparison it is deduced that the spiral ($m=1$) fluctuations observed to develop after the classical expansion of a heat plume corresponds to a drift-Alfvén mode. Further comparisons that elucidate the subsequent nonlinear behavior and development of anomalous transport are worth pursuing.

ACKNOWLEDGMENTS

This work is sponsored by the Office of Naval Research and by the U.S. Department of Energy. The authors thank Dr. A.T. Burke for valuable discussions concerning the temperature striation experiments.

APPENDIX A: COLLISIONAL ELECTRON RESPONSE

Here, we outline the derivation of Eq. (8). We assume that the perturbed part of the electron distribution function evolves according to Eq. (5) and expand f_{1e} as a series of Legendre polynomials

$$f_{1e}=\sum_{n=0}^{\infty} a_n(v,r)P_n(\mu). \tag{A1}$$

Taking the appropriate moment of f_{1e} and exploiting the orthogonality of the Legendre polynomials, the parallel current density carried by the electrons is

$$j_{1ze}=-\frac{4\pi}{3}e\int_0^{\infty} v^3 a_1(v,r)\,dv. \tag{A2}$$

Substituting Eq. (A1) into Eq. (5) leads to the recursion relation

$$a_{n+1}b_{n+1}+a_n d_n+a_{n-1}b_n=S(v,r), \tag{A3}$$

where the coefficients b_n and d_n are defined by

$$b_n=\frac{ik_z v\, n}{(2n-1)(2n+1)},\quad d_n=-\frac{i\omega+\nu(v,r)n(n+1)}{2n+1} \tag{A4}$$

and

$$S(v,r)=\int_{-1}^{1} d\alpha\left[\frac{e}{m}E_{1z}\frac{\partial f_{e0}}{\partial v_z}-\nabla_\perp\cdot(\mathbf{v}_\perp f_{e0})\right]\frac{P_n(\alpha)}{2}. \tag{A5}$$

Using Eq. (6) to evaluate the perpendicular guiding center velocity in Eq. (A5), the integrand in $S(v,r)$ can be separated into terms proportional to P_0 and P_1. Carrying out the integration over μ yields

$$S(v,r)=A_0(v,r)\,\delta_{0,n}+\tfrac{1}{3}A_1(v,r)\,\delta_{1,n}, \tag{A6}$$

where

$$A_0=-\frac{c}{B_0}\left(E_{1\theta}\frac{\partial}{\partial r}f_{0e}+ik_0 f_{0e}B_{1z}\right), \tag{A7}$$

$$A_1=-\frac{B_{1r}}{B_0}v\frac{\partial}{\partial r}f_{0e}+\frac{B_{1z}}{B_0}ik_z v f_{0e}-\frac{ev}{m\overline{v_e^2}}E_{1z}f_{0e}. \tag{A8}$$

Substituting Eqs. (A6) and (A8) into Eq. (A3) and solving for the coefficient a_1 yields

$$a_1=\frac{(A_1/3)-(b_1/d_0)A_0}{d_1-(b_1^2/d_0)+b_2(a_2/a_1)}, \tag{A9}$$

$$=\frac{v/(B_0)(\partial f_{0e}/\partial r)[B_{1r}+(k_z/k_0)E_{1\theta}]+ev/(m\overline{v_e^2})E_{1z}f_{0e}}{i\omega[1+2\nu(v,r)/(i\omega)-(1/3)(k_z v/\omega)^2-(2/5)(k_z v/\omega)(a_2/a_1)]}. \tag{A10}$$

Substituting Eqs. (15) and (14) into Eq. (A10) shows that a_1 is simply proportional to E_{1z}, i.e.,

$$a_1=\frac{1}{i\omega D_\nu}\left[\frac{k_\theta v}{k_0 B_0}\frac{\partial}{\partial r}f_{0e}+\frac{ev}{m\overline{v_e^2}}f_{0e}\right]E_{1z}, \tag{A11}$$

where $k_\theta=m/r$

$$D_\nu\equiv 1+2\nu(v,r)/(i\omega)-(1/3)(k_z v/\omega)^2-(2/5)(k_z v/\omega)\times(a_2/a_1), \tag{A12}$$

and (a_2/a_1) is a continued fraction defined by

$$\frac{a_n}{a_{n-1}}=\frac{-b_n}{d_n+b_{n+1}(a_{n+1}/a_n)}. \tag{A13}$$

Substituting Eq. (A11) into Eq. (A2) gives

$$j_{1ze}=\left[\left(\frac{\omega_{pi}}{k_z c_s}\right)^2\frac{1}{2\omega}\frac{k_\theta c_s^2}{\Omega_i}\left(\frac{8\pi k_z^2}{3\omega^2}\int_0^\infty dv\,\frac{(v^4/n_0)(\partial f_{0e}/\partial r)}{D_\nu}\right)+\left(\frac{\omega_{pe}}{\sqrt{2}k_z\overline{v_e}}\right)^2\left(\frac{8\pi k_z^2}{3\omega^2}\int_0^\infty dv\,\frac{(v^4/n_0)f_{0e}}{D_\nu}\right)\right]\left(\frac{i\omega}{4\pi}\right)E_{1z}. \tag{A14}$$

If f_{0e} is given by Eq. (7) then

$$\frac{\partial}{\partial r}f_{0e}=\frac{\partial n_0(r)}{\partial r}\hat{f}_0(v,r)+\left(\frac{v^2}{2\overline{v_e^2}(r)}-\frac{3}{2}\right)\times\frac{n_0(r)}{T_e(r)}\frac{\partial T_e(r)}{\partial r}\hat{f}_0(v,r), \tag{A15}$$

where $f_{0e}=n_0(r)\hat{f}_0$, and Eq. (A14) becomes Eq. (8).

APPENDIX B: POTENTIAL FORMULATION

Here, we present an alternative formulation of the present problem in terms of the scalar and vector potentials, ϕ_1 and $\mathbf{A}_1$. Assuming that the perpendicular electric field is electrostatic (i.e., $\mathbf{A}_\perp=0$), the wave fields can be expressed as

$$\mathbf{E}_1=-\nabla_\perp\phi_1+ik_0A_{1z}\hat{z}, \tag{B1}$$

$$\mathbf{B}_1=\nabla\times\mathbf{A}_1. \tag{B2}$$

The system of equations governing the behavior of ϕ_1 and A_{1z} is derived from the quasineutrality condition ($n_{1e}\approx n_{1i}$) and the parallel component of Ampere's law

$$\nabla^2A_{1z}=-\frac{4\pi}{c}j_{1z}, \tag{B3}$$

where the displacement current has been neglected.

For simplicity, we calculate the fluctuating densities and currents assuming a collisionless plasma. The perturbed distribution function of charge species α is assumed to evolve according a linearized drift kinetic equation [e.g., Eq. (5) with $\nu_{ei}=0$] and can be solved for explicitly. The density and current fluctuations are easily obtained by taking the appropriate moments of $f_{1\alpha}$. In terms of ϕ_1 and A_{1z}, they are

$$n_{1\alpha}=\frac{k_\theta c}{B_0}\frac{\partial}{\partial r}\left[\frac{n_0}{\sqrt{2}k_z\overline{v_e}}Z(\zeta_\alpha)\right]\phi_1+\frac{c}{\Omega_\alpha B_0}\left[\frac{1}{r}\frac{\partial}{\partial r}\left(rn_0\frac{\partial}{\partial r}\phi_1\right)-k_\theta^2n_0\phi_1\right]-\frac{k_\theta}{k_zB_0}A_{1z}\frac{\partial}{\partial r}\{n_0[1+\zeta_\alpha Z(\zeta_\alpha)]\}+\frac{q_\alpha n_0}{2k_zm_\alpha\overline{v_\alpha^2}}Z'(\zeta_\alpha)(k_z\phi_1-k_0A_{1z}) \tag{B4}$$

and

$$j_{1z\alpha}=\left\{\frac{q_\alpha ck_\theta}{k_z^2B_0}\frac{\partial}{\partial r}[(1+\zeta_\alpha Z(\zeta_\alpha))n_0]+\frac{q_\alpha^2n_0}{m\omega}\zeta_\alpha^2Z'(\zeta_\alpha)\right\}\times(k_z\phi_1-k_0A_{1z}). \tag{B5}$$

In evaluating n_{1i} and j_{1zi}, the approximation is made that the ion response to the oscillating fields is that of a cold fluid, so that $Z(\zeta_i)$ can be expanded for large argument.

Using Eqs. (B4) and (B4) in the quasineutrality condition and Eq. (B3) then yield the desired eigenvalue equations

$$\frac{1}{r}\frac{\partial}{\partial r}\left(r\epsilon_\perp\frac{\partial}{\partial r}\phi_1\right)-k_\theta^2\epsilon_\perp\phi_1-ik_z\psi(r,\omega)(-ik_z\phi_1+ik_0A_{1z})=0, \tag{B6}$$

$$\frac{1}{r}\frac{\partial}{\partial r}\left(r\frac{\partial}{\partial r}A_{1z}\right)-k_\theta^2 A_{1z}-ik_0\psi(r,\omega)(-ik_z\phi_1+ik_0A_{1z})=0 \tag{B7}$$

where the function

$$\psi(r,\omega)=\epsilon_\parallel+\left(\frac{\omega_{pe}}{k_z\overline{v_e}}\right)^2\frac{\omega_*}{\omega} \tag{B8}$$

characterizes the kinetic plasma response. Here, $\epsilon_\perp$ and $\epsilon_\parallel$ are the same quantities defined in Sec. II, but with the contribution from the displacement current (i.e., unity) neglected.

Next, we show that this potential formulation can be directly recovered from the more general field formulation. However, note that simply setting $B_{1z}=0$ in Eqs. (17) and (18) does not recover Eqs. (B6) and (B7). To properly recover the potential formulation, it is necessary to first eliminate B_{1z} from Eqs. (17) and (18) using Eqs. (13)–(16). This leads to

$$\frac{1}{r}\frac{\partial}{\partial r}(r\epsilon_\perp E_{1r})+ik_\theta\epsilon_\perp E_{1\theta}+ik_z\psi(r,\omega)E_{1z}=0, \tag{B9}$$

$$\frac{1}{r}\frac{\partial}{\partial r}\left(r\frac{\partial}{\partial r}E_{1z}-ik_z rE_{1r}\right)-k_\theta(k_\theta E_{1z}-k_z E_{1\theta})+\psi(r,\omega)E_{1z}=0, \tag{B10}$$

which reduce to Eqs. (B6) and (B7) when Eq. (B1) is used to eliminate $\mathbf{E}_1$.

In the local limit, Eqs. (B6) and (B7) yield the dispersion relation

$$\frac{\overline{\beta}}{2}\left(\frac{k_\theta c}{\omega_{pe}}\right)^2+\left(\frac{\omega^2}{k_z^2v_A^2}-1\right)\left[\frac{\omega_*}{\omega}+\frac{1}{2}Z_N(\zeta_e)\right]=0. \tag{B11}$$

A similar dispersion relation has been used by Fredrickson and Bellan to investigate drift-Alfvén waves in a research tokamak.[17] Lastly, we note that the terms on the rhs (right-hand-side) of Eq. (B11) are exactly the terms within the first set of braces in Eq. (21) which give rise to local shear-Alfvén solutions.

[1] M. C. Kelley, T. L. Arce, J. Salowey, M. Sulzer, W. T. Armstrong, M. Carter, and L. Duncan, J. Geophys. Res. **100**, 17367 (1995).
[2] P. M. Kintner, J. Vago, S. Chesney, R. L. Arnoldy, K. A. Lynch, C. J. Pollock, and T. E. Moore, Phys. Rev. Lett. **68**, 2448 (1992).
[3] A. I. Eriksson, B. Holback, P. O. Dovner, R. Bostrom, G. Holmgren, M. Andre, L. Eliasson, and P. M. Kintner, Geophys. Res. Lett. **21**, 1843 (1994).
[4] S. J. Zweben and S. S. Medley, Phys. Fluids B **1**, 2058 (1989).
[5] N. J. Lopes Cardozo, F. C. Schuller, C. J. Barth, C. C. Chu, F. J. Pipjer, J. Lok, and A. A. Oomens, Phys. Rev. Lett. **73**, 256 (1994).
[6] K. J. Reitzel and G. J. Morales, Phys. Plasmas **3**, 3251 (1996).
[7] R. A. Koch and Jr. W. Horton, Phys. Fluids **18**, 861 (1975).
[8] A. Y. Wong, G. J. Morales, D. Eggleston, J. Santoru, and R. Behnke, Phys. Rev. Lett. **47**, 1340 (1981).
[9] G. J. Morales, S. N. Antani, and B. D. Fried, Phys. Fluids **28**, 3302 (1985).
[10] J. F. Bamber, J. E. Maggs, and W. Gekelman, J. Geophys. Res. **100**, 23795 (1995).
[11] W. Gekelman, H. Pfister, Z. Lucky, J. Bamber, D. Leneman, and J. Maggs, Rev. Sci. Instrum. **62**, 2875 (1991).
[12] J. E. Maggs and G. J. Morales, Phys. Plasmas **4**, 290 (1997).
[13] A. T. Burke, J. E. Maggs, and G. J. Morales, Phys. Rev. Lett. **81**, 3659 (1998).
[14] G. Schmidt, in *Physics of High Temperature Plasmas*, 2nd ed. (Academic, New York, 1979), Chap. 10, p. 355.
[15] B. D. Fried and S. D. Conte, *The Plasma Dispersion Function* (Academic, New York and London, 1961).
[16] J. R. Peñano, G. J. Morales, and J. E. Maggs, Phys. Plasmas **4**, 555 (1997).
[17] E. D. Fredrickson and P. M. Bellan, Phys. Fluids **28**, 1866 (1985).
[18] V. D. Shavranov, in *Reviews of Plasma Physics*, edited by M. A. Leontovich (Consultants Bureau, New York, 1966), Vol. 2, p. 103.
[19] W. H. Press, S. A. Teukolsky, W. T. Vetterling, and B. P. Flannery, in *Numerical Recipes in Fortran*, 2nd ed. (Cambridge University Press, New York, NY, 1992), Chap. 17, p. 745.
[20] R. F. Ellis and R. W. Motley, Phys. Fluids **17**, 582 (1974).
[21] E. Marden-Marshall, R. F. Ellis, and J. E. Walsh, Plasma Phys. Controlled Fusion **28**, 1461 (1986).